Available online at www.sciencedirect.com
SCIENCE DIRECT®
Journal of Nuclear Materials 355 (2006) 10–20
journal of nuclear materials
www.elsevier.com/locate/jnucmat

A detailed study of UO_2 to U_3O_8 oxidation phases and the associated rate-limiting steps

G. Rousseau [a,b,c,d], L. Desgranges [a,*], F. Charlot [b], N. Millot [b], J.C. Nièpce [b], M. Pijolat [c], F. Valdivieso [c], G. Baldinozzi [d], J.F. Bérar [e]

[a] CEA Cadarache, DEN/DEC/SA3C/L2EC Bât. 316, 13108 St. Paul-lez-Durance, France
[b] LRRS, Equipe MANAPI, UMR 5613 CNRS-Université de Bourgogne, 9 Av. Alain Savary, BP 47870, 21078 Dijon, France
[c] LPMG, Ecole Nationale Supérieure des Mines de St-Etienne, Centre SPIN, Equipe PROCESS, 158 Cours Fauriel, 42023 St-Etienne cedex 2, France
[d] SPMS, UMR 8580 CNRS-Ecole Centrale Paris, Grande Voie des Vignes, 92295 Châtenay-Malabry, France
[e] D2AM CRG, CNRS, ESRF–Polygone Scientifique Louis Néel, 6 rue Jules Horowitz, 38000 Grenoble, France

Received 21 February 2005; accepted 25 March 2006

Abstract

The kinetic and crystalline evolutions of UO_2 during its oxidation into U_3O_8 at 250 °C in air were studied by isothermal thermogravimetry and calorimetry, coupled with an in situ synchrotron X-ray diffraction on the D2AM-CRG beamline at ESRF. This study was aimed at determining experimentally the validity of the kinetic assumptions made in existing literature to account for the oxidation of UO_2 into U_3O_8 and also to determine precisely the structural evolution, in relation to the kinetic behaviour. Our results provide evidence of four distinct kinetic time domains, and the assumption of a single rate-limiting step is verified only for two of them. The crystalline phases associated with these domains are also identified. In fact, the first kinetic domain corresponds to the reaction of UO_2 into U_4O_9; the second one is linked to the two simultaneous reactions, UO_2 into U_4O_9 and U_4O_9 into U_3O_7. Finally, the transition from U_3O_7 into U_3O_8 corresponds to the third and fourth kinetic domains. These results show that the oxidation of UO_2 into U_3O_8 cannot satisfactorily be described with modelling approaches used in the literature. A new general outline is proposed to study the oxidation of uranium oxides. This outline will improve both the understanding and predictions of oxidation processes at the relatively low temperatures that are expected during interim storage of spent nuclear fuel.

1. Introduction

In the framework of dry interim storage of nuclear fuel, accident scenarios consider a failure of the container and of the cladding that would put the nuclear ceramic in contact with atmosphere. The U_3O_8 formation due to UO_2 oxidation leads to a 36% volume increase [1] that will lead to a severe damage of the fuel rod. In this context, it is necessary to make predictions on the oxidation kinetics of UO_2 for time intervals up to several 100 years, which are significantly longer than the available

* Corresponding author. Tel.: +33 4 42 25 31 59; fax: +33 4 42 25 36 11.
E-mail address: lionel.desgranges@cea.fr (L. Desgranges).

0022-3115/$ - see front matter © 2006 Elsevier B.V. All rights reserved.
doi:10.1016/j.jnucmat.2006.03.015

experiment time intervals. During long-term storage, the temperature at the start, and during a number of years thereafter appears to be greater than 200 °C for a UO_2 LWR fuel and 300 °C for a MOX fuel. Thus, the modelling should rely on the actual mechanisms and on the true phases occurring during the oxidation.

Up to now, it was generally accepted that the oxidation of uranium dioxide at temperatures below 400 °C was a two-step reaction, as proposed in 1957 by Aronson et al. [2,3]:

$$UO_2 \rightarrow U_4O_9/U_3O_7 \rightarrow U_3O_8 \quad (1)$$

However, the structural mechanism responsible for the isothermal transformation of UO_2 into U_3O_8 seems also unclear. In Eq. (1), McEachern and Taylor used the term U_4O_9/U_3O_7 to refer to the product of the first stage of air oxidation of UO_2 [3]. Several intermediate oxidation products have been reported, namely UO_{2+x} [4,5], U_4O_9 [5], γ-U_4O_9 [6], α-U_3O_7 [5,7], β-U_3O_7 [5,7] and γ-U_2O_5 [8], whose crystallographic structures are not well established. These crystalline structures are derivatives of UO_2. In the case of the oxidation of UO_2 powders, it is generally accepted that the first stage of oxidation is the incorporation of small quantities of oxygen into the fluorite-type lattice to form hyperstoichiometric UO_{2+x}. The solubility of oxygen in this phase depends on the temperature [4,5]. Then, the oxidation of UO_2 powders involves U_3O_7 formation. In the literature, two tetragonal phases are reported, α-U_3O_7 and β-U_3O_7 [5,7], which only differ from their c/a ratio, respectively 0.989 and 1.031 [7]. Typically, α-U_3O_7 is considered as the normal result of the oxidation at temperatures less than 200 °C [3], whereas β-U_3O_7 appears at temperatures higher than 200 °C [3,7]. It is noted that some studies report intermediate tetragonal phases with c/a ratios ranging between those of α-U_3O_7 and β-U_3O_7 [6,9]. Finally, the oxidation of powders proceeds only from β-U_3O_7 to U_3O_8, and not from α-U_3O_7 [7]. The U_3O_8 crystalline structure is orthorhombic. In the case of the oxidation of sintered pellets, the intermediate product is β-U_3O_7 [6,9] and the formation of a tetragonal phase with c/a ratio less than 1 has not been previously reported. Concerning the oxidation of spent fuel, the main fact is that the intermediate oxidation product is a cubic phase often described as U_4O_9-type, but with an O/U ratio that may exceed that for U_3O_7 phase [6].

On the basis of the thermal gravimetric analysis and X-ray diffraction data, there is a general agreement that the parabolic kinetics for the formation of U_4O_9/U_3O_7 on UO_2 powders indicates a diffusion-controlled mechanism, whereas the sigmoidal reaction kinetics observed for the formation of U_3O_8 is generally interpreted in terms of a nucleation and growth reaction mechanism. The mechanism for the rate of U_3O_8 formation has been widely studied [1–3,10,11]. However a recent review [3] shows a significant degree of uncertainty in estimates for both the rate and the activation energy of a nucleation and growth mechanism. Thus the U_3O_8 formation process is not yet well understood.

Since the Aronson paper, the modelling of the oxidation of UO_2 into U_3O_8 is based on the assumption that the reaction rate can be written as

$$\frac{d\alpha}{dt} = A \exp\left(-\frac{E_a}{RT}\right) f(\alpha), \quad (2)$$

where α is a dimensionless fractional conversion function of time, A is called the pre-exponential factor, E_a is the activation energy and $f(\alpha)$ is an analytical function (which depends on the shape of the grains and the step controlling the growth [12,13]). The transformation of UO_2 into U_4O_9/U_3O_7 is interpreted using the Jander's law [3,13,14], in which the function $f(\alpha)$ is

$$f(\alpha) = 3/2(1-\alpha)^{2/3}[1-(1-\alpha)^{1/3}]^{-1}. \quad (3)$$

However, Schmalzried [15] has pointed out the fact that this law (sometimes referred as the D_3-law [12]) has no physical meaning, excepted in the very beginning of reactions in which the product layer may be considered as a plane. The rigorous mathematical law describing the growth of a product layer inward spherical grains, the growth rate-limiting step being the diffusion of chemical species inside the product layer, is the Ginstling–Brounshtein law [13,16], often denoted as the D_4 law (or the more general Carter–Valensi law [13,17,18], which takes into account the differences in the molar volumes of reactant and product).

The sigmoidal part of kinetic curves for $\alpha(t)$ corresponding to the oxidation of U_3O_7 into U_3O_8 is usually accounted for with the Avrami–Erofeev model [3,13,19,20] (also referred as Johnson–Mehl model [21]), the function $f(\alpha)$ being then

$$f(\alpha) = n(1-\alpha)[-\ln(1-\alpha)]^{1-1/n} \quad (4)$$

in which the parameter 'n' is an empirically determined constant. Nevertheless, in the Avrami–Erofeev's model, it is assumed that the nucleation can occur in the whole volume of the grains. But, in solid-state reactions, it is commonly admitted that nuclei appear at the surface of the solids, and thus the Avrami's model is not appropriate. In the general case, Eq. (1) implies that the rate is controlled by a reaction step that follows the Arrhenius law (this is not always the case, for example when an adsorption step is involved, the reaction step may follow a Langmuir isotherm). Eq. (1) also implies that the rate is fixed by the value of α ($f(\alpha)$), which may not be the case, particularly when nucleation and growth processes are in competition or when the specific surface changes during the reaction.

Consequently, we propose a more general expression for the rate [22,23] given by Eq. (5)

$$\frac{d\alpha}{dt} = \Phi(T, P_i)E(t) \quad (5)$$

in which Φ is a rate per unit area (mol m^{-2} s^{-1}). The function Φ depends on the nature of the rate-limiting step (diffusion, interface reaction), it is independent of time but may be a function of temperature T and thermodynamic chemical potential of the reacting gases P_i. The function $E(t)$ (in m^2 mol^{-1}) corresponds to the extent of the reaction zone where the rate-limiting step is located. Expression of Eq. (5) only assumes the existence of a rate-limiting reaction step, but no additional assumption is made concerning the nature and the spatial localisation of the reaction step.

The purposes of this work are to experimentally determine the validity of the kinetic assumptions generally made to account for the oxidation of UO_2 into U_3O_8, with a previously established methodology [24,25], and to determine precisely the crystalline structural evolution in relation to the kinetic behaviour. This methodology allows to verify:

(i) the pseudo-stationary state assumption (which is necessary to assume the existence of a rate-limiting step). It can be verified by measuring the reaction rate with two techniques (for example, simultaneous thermogravimetry and calorimetry [24–27]): if the system proceeds in a pseudo-stationary state, the rates of weight gain and the heat flow should remain proportional during all the reaction,

(ii) the assumption of a single rate-limiting step, and thus the validity of Eq. (5). This can be verified using a method based on jumps of temperature or pressure [24–27].

Our results provide data of four distinct kinetic domains during the oxidation of UO_2 up to U_3O_8. The assumption of a single rate-limiting step is verified only for two of them. The crystalline phases associated to these domains were also identified.

2. Experimental

The uranium dioxide test specimens used in this study were from a batch of depleted UO_2 powder, whose stoichiometry is close to $UO_{2.02}$ and grain size ranges from 2 to 10 μm. In order to simulate the storage conditions, the oxidation experiment was carried out at 250 °C in gas mixture with O_2 partial pressure ≈0.2 atm, the other mixing gas depending on the apparatus used (atmospheric air for X-ray diffraction, nitrogen or helium mixing for thermogravimetry). For these tests, no special care was given to control humidity since it has little influence on UO_2 oxidation at temperature higher than 200 °C [3].

The in situ synchrotron X-ray powder diffraction experiments were performed on the D2AM-CRG beam line ($\lambda = 0.154864$ nm) at ESRF. Test samples were positioned to form a fixed angle of 10° with the impinging beam. During the oxidation of UO_2 into U_3O_8, most of the in situ diffraction patterns were recorded every 20 min. The temperature of the sample was changed during the experiment in order to get valuable information for each observed crystalline phase within the allocated time.

The in situ classical X-ray diffraction experiments were conducted using an INEL diffractometer equipped with a curved position-sensitive detector (CPS 120 INEL). Monochromatic Co-Kα_1 X-rays ($\lambda = 0.17889$ nm) were obtained with a primary focusing Ge monochromator. Thermal treatments are provided with a high temperature furnace developed at LRRS. The full 2θ range over which data were collected for both the synchrotron and conventional XRD was from 20° to 80°.

The experiments of simultaneous calorimetry and thermogravimetry were performed using a thermoanalyser SETARAM TG DSC 111 under a flowing mixture of helium and oxygen to test the pseudo-stationary state assumption. The sample was first heated in helium to 250 °C and, after reaching this

reaction temperature, a mixture of helium and oxygen was introduced into the balance to attain an oxygen partial pressure of 0.2 atm. A constant gas flow rate of 0.03 l per minute was maintained throughout the experiments.

The weight gain data needed for temperature jump tests were obtained from isothermal thermogravimetric experiments using a SETARAM TAG24 microbalance with a mass sensibility of about 0.001%. The experimental apparatus has continuous recording of the change in sample weight as a function of time in a controlled gaseous atmosphere. The sample was first heated in a nitrogen atmosphere until the desired reaction temperature (250 °C) was reached and, after that, air (0.2 atm O_2) was introduced into the balance. A constant airflow rate of 0.16 l min^{-1} was maintained throughout the experiments. When the desired oxidation time is reached, the oxidation temperature was suddenly changed from 250 °C to 280 °C. The jump temperature tests was performed at several oxidation times.

3. Kinetic study

3.1. Shape of the kinetic curves

Fig. 1 shows thermal gravimetric curve as a function of time recording during the oxidation of UO_2 into U_3O_8 at 250 °C under nitrogen–oxygen mixture. Fig. 1 is a typical isothermal gravimetric curve versus the time for the oxidation of UO_2 powders. The oxidation curve consists of two steps: first, a parabolic reaction is observed until an O/U ratio closed to 2.33 is reached, this corresponds to the intermediate product U_4O_9/U_3O_7. At this ratio, a plateau is observed. Then, a sigmoidal second reaction step begins during which the formation of U_3O_8 phase ($O/U \approx 2.67$) occurs, but the U_3O_8 phase transformation is not totally completed in 25 h at 250 °C.

3.2. Pseudo-stationary state assumption

Fig. 2 represents the variations of the rate of weight gain (dm/dt) and the heat flow (dQ/dt) versus time, at 250 °C in helium–oxygen mixture. The results show clearly that the curves are well superimposed although some differences seem to appear at the end of the oxidation. Thus, it can be concluded that the system is in a pseudo-stationary state throughout the main stages of the reaction.

3.3. Rate-limiting step assumption

If a rate-limiting step exists, Eq. (5) gives the variations of the oxidation rate with the intensive variables ($T, P_i, \ldots$) and the time. Eq. (5) involves the fractional conversion (α), which is usually defined for a single reaction step. In the case of the oxidation of UO_2, the literature data show that there are at least two reaction steps, and it is not possible to deduce the fractional conversion of each one separately from the weight gain curves. Thus, we prefer to write Eq. (6) using the mass variation Δm, according to

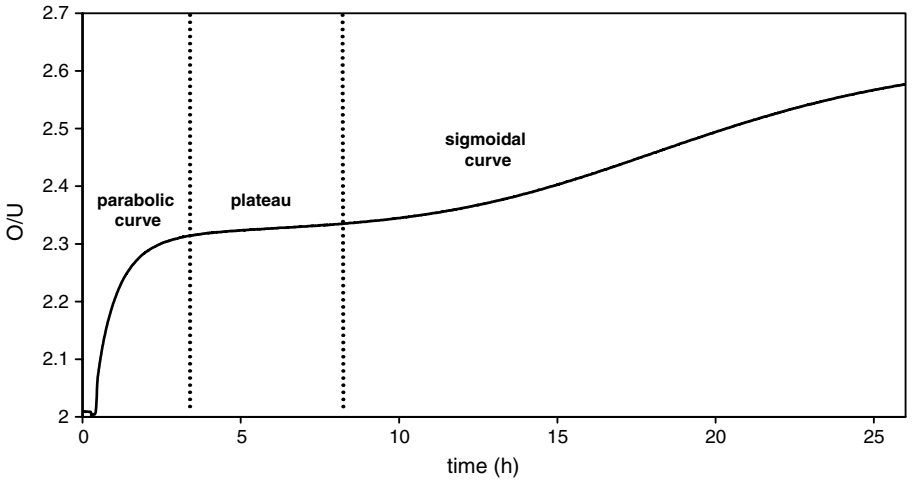

Fig. 1. Thermal gravimetric curve as a function of time recording during the oxidation of UO_2 into U_3O_8 at 250 °C under air atmosphere (0.2 atm O_2).

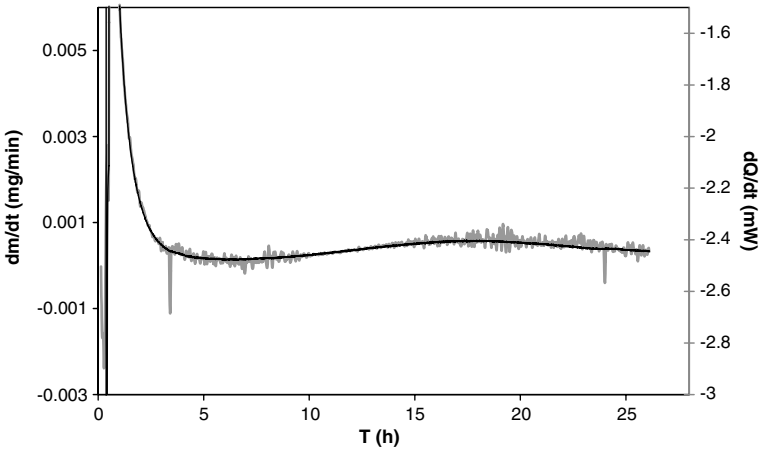

Fig. 2. Heat flow and rate of weight gain versus time.

$$\frac{\mathrm{d}(\Delta m)}{\mathrm{d}t} = n_0 \Phi(T, P_i) E(t), \tag{6}$$

where parameter 'n_0' is a constant with the unity of a mass. Eq. (6) can be tested by experiments based on the sudden jump method, which consists of changing suddenly a physico-chemical variable (temperature or pressure) from a value X_0 to X_1, at a given oxidation time [22–25].

In our experiments, the oxidation temperature was raised abruptly from T_0 (250 °C) to T_1 (280 °C) at different times, t_i, during the oxidation process of UO_2 to U_3O_8. Then, from Eq. (6), the rates before and after the temperature jump at the oxidation time t_i, respectively R_l and R_r, can be written [14]:

$$R_l = \left(\frac{\mathrm{d}\Delta m}{\mathrm{d}t}\right)_l = n_0 \Phi(T_0) E(t_i) \quad \text{and}$$

$$R_r = \left(\frac{\mathrm{d}\Delta m}{\mathrm{d}t}\right)_r = n_0 \Phi(T_1) E(t_i).$$

The ratio of the above expressions is

$$\frac{R_r}{R_l} = \frac{n_0 \Phi(T_1) E(t_i)}{n_0 \Phi(T_0) E(t_i)} = \frac{\Phi(T_1)}{\Phi(T_0)}. \tag{7}$$

For a set of prescribed oxidation experiments, one selects arbitrarily a set of times t_i ($t_1, t_2, t_3, \ldots$) at which a sudden jump in temperature (T_0 to T_1) is to be imposed. So, if the pseudo-stationary state and the rate-limiting step assumption are verified (for the seek of simplicity we will say if the 'ΦE' test is verified), then the ratio R_r/R_l are equal to each other for any time t_i. If these ratio ar not equal to each other (if the 'ΦE' test is not verified), Eq. (6) cannot be considered as valid and the single rate-limiting step assumption is not verified.

Fig. 3 shows two typical curves that were obtained in this study. Both Fig. 3(a) and (b) show the sudden jump of temperature from 250 °C to 280 °C. In Fig. 3(a) the time of the temperature jump was at 30 min. In Fig. 3(b), the time of the

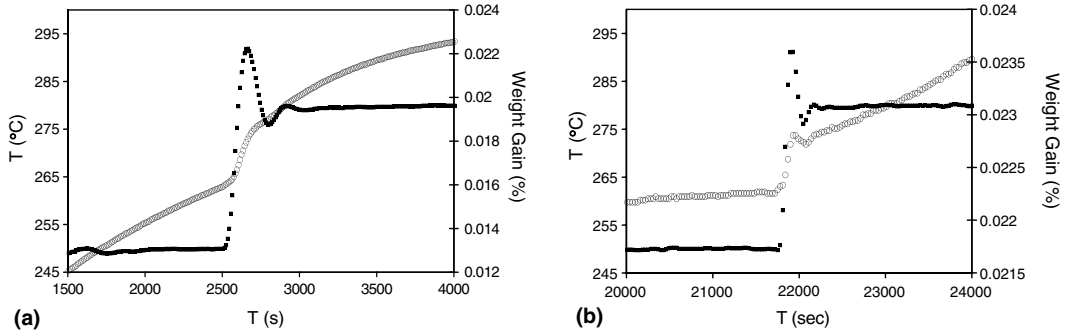

Fig. 3. Jumps of temperature from 250 °C to 280 °C (square) and corresponding evolution of the weight gain curve (circle): (a) oxidation time: 30 min, (b) oxidation time: 6 h.

temperature jump was at 4 h. Note that the slope of R_r and R_l are different in the two cases.

From Fig. 3(a), the ratio of the rate before the temperature jump R_l to the one after the temperature jump R_r is calculated on time increments of 200 s for oxidation times that are less than 2 h, whereas the more progressive weight gain observed for higher oxidation times in Fig. 3(b), are calculated on time increments of 500 s. As can be seen in Fig. 3, there is a temperature transient during the temperature jump. Because of this temperature transient, a precise determination of the activation energy is not possible based on experimental values of the R_r/R_l ratio. In fact, a variation of only ±5 °C can induce an uncertainty on the activation energy of about ±10–20 kJ/mol.

In Fig. 4, the R_r/R_l ratios, evaluated from experimental data are plotted versus temperature jump time. On the same figure, the weight gain curve is plotted versus time for a constant temperature (250 °C) oxidation experiment with nitrogen–oxygen gas mixture. Note that the values of the R_r/R_l ratios depend on the temperature jump time t_i.

The evolution of the R_r/R_l ratios in Fig. 4 provides evidence of four different kinetic domains, denoted as I–IV. At the beginning, for oxidation times less than to 2 h (domain I), which corresponds to a very fast weight gain time domain, the ratio is constant, with a value of 1.3 ± 0.1. This result shows that the 'ΦE' test is verified for time domain I. For oxidation time between 2 and 6 h (domain II), the R_r/R_l ratios increase continuously from 1.7 ± 0.1 to 6.0 ± 0.2. Unlike the first domain, this variation indicates that the 'ΦE' test is not verified for time domain II. In domain III, between 6 and 14 h, a constant value, 7.6 ± 0.2, of the R_r/R_l ratios is observed and the 'ΦE' test is verified. Finally, between 14 and 24 h (domain IV), the R_r/R_l ratios change from 7.1 ± 0.2 to 5.6 ± 0.2 and the 'ΦE' test is not verified. So, the 'ΦE' test experiments bring into evidence four different kinetic domains during the oxidation of UO_2 into U_3O_8. Moreover, the experimental R_r/R_l ratios show that the 'ΦE' test is only verified for two of them.

These kinetic results show that a rate-limiting step approximation to model oxidation seems only valid in two short time domains of weight gain. These data suggest that the oxidation of UO_2 cannot be fully described with models using only two successive oxidation reactions. In order to improve existing models it is necessary to know which crystalline phases correspond to each time domain.

4. In situ X-ray diffraction – phase determination

4.1. Methods

The current reference crystallographic data (mainly from ex situ experiments) present large discrepancies and they do not provide a clear interpretation of the crystallographic changes occurring during the oxidation of UO_2 into U_3O_8 [3]. Table 1 summarizes some available crystallographic data for these phases. Given the existing literature, two sets of X-ray diffraction experiments were conducted to better clarify the crystallographic sequence:

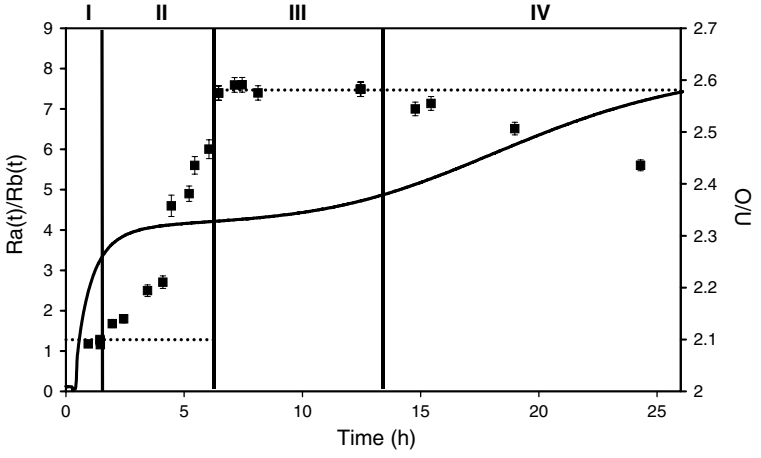

Fig. 4. Weight gain curve and R_r/R_l ratios.

Table 1
Crystallographic properties of the main uranium oxides

Phases	Crystallographic properties	References
UO_2	SG: Fm-3 m, fluorite structure, $a = 0.547$ nm	[28]
U_4O_9	SG: unknown, fluorite fourfold superstructure, $a \approx 2.176$ (4×0.544) nm	[29]
U_3O_7	SG: unknown, tetragonal distortion of the cubic cell, α-U_3O_7: $c/a = 0.989$ and β-U_3O_7: $c/a = 1.031$	[7]
U_3O_8	SG: C2mm, orthorhombic structure, $a = 0.672$ nm, $b = 1.196$ nm, $c = 0.415$ nm	[30]

(1) an in situ synchrotron diffraction study at ESRF conducted in non-strict isothermal conditions in order to identify the crystalline phases,
(2) an in situ classical X-ray diffraction performed in strict isothermal conditions at 250 °C to compare the structural results with the kinetic ones.

All the diffraction patterns recorded at ESRF during the oxidation of UO_2 into U_3O_8 were refined using the Rietveld method [31] with the JANA program of Petricev and Dusek [32]. The Rietveld analysis can also provide interesting information on cell parameters and on the profile shapes of the diffraction peaks. In the case of the synchrotron diffraction, it is generally verified that the width of the diffraction peaks does not depend on instrumental factors, but almost exclusively on crystallite size and strain effects. The broadening induced by the finite diffracting crystallite size τ and by the microstrain ε, are expressed respectively by Eqs. (7) and (8):

$$\beta_{\text{size}} = \frac{\lambda}{\tau \cos\theta}, \tag{8}$$

$$\beta_{\text{microstrain}} = \varepsilon \tan\theta, \tag{9}$$

where β is the integral breadth, λ the wavelength, τ the crystallite size and ε the microstrains [33].

For the crystallographic data presented in Table 1, the space groups used for UO_2 and U_3O_8 analysis were respectively Fm-3m and C2mm. U_4O_9 is known to crystallise into a closely related fluorite structure as UO_2, but the same simpler cubic space group was used in our phase description. On the other hand, in order to take into account tetragonal distortion, which appears with the formation of U_3O_7, the U_3O_7 phase was analysed with the I4/mmm space group.

4.2. Results

Fig. 5 shows the crystalline structural evolution obtained from ESRF experiments during the oxidation of UO_2 into U_3O_8 at 250–260 °C in atmospheric air in the 2θ angle range 27–35°. It was necessary to heat the sample above 250 °C in order to fit the entire data collection within the allotted synchrotron beam-time. The initial powder of UO_2 has a cell parameter of 0.5464(2) nm, in agreement with the average value of 0.5470 nm reported in the literature [28,34]. The average diffracting crystallite size is about 250 nm. During the first steps of the oxidation, the profile of the initial UO_2 powder does not seem to evolve.

Then, a simultaneous splitting of all the diffraction peaks is clearly observed in Fig. 5. In the literature, it is generally accepted that the product formed in these early stages of the oxidation reaction is α-U_3O_7, a tetragonal phase. This hypothesis would induce a splitting of the 200 peak, but not of the 111 peak as observed in our experiment. Therefore, this intermediate phase is a cubic phase with a cell parameter smaller than UO_2. The term U_4O_{9-y} is generally used to describe this phase and it actually corresponds to the cubic phase already reported in the literature and characterized by a unit cell smaller than UO_2 [28]. This U_4O_{9-y} cubic phase has a cell parameter of 0.5451(2) nm. This cell parameter gradually decreases to 0.5441(2) nm as the oxidation proceeds, because of the progressive incorporation of oxygen into the fluorite lattice of UO_2. The diffraction peaks of U_4O_{9-y} are much broader than the UO_2 peaks, possibly representative of stoichiometric core regions in the grains. In particular, the anisotropic broadening of the (200) peak can be explained by an increased microstrain of about 2% along this direction. This first transition leads to an overall small decrease (0.7%) of the cell volume compared to the stoichiometric UO_2 cell volume.

Following the literature, the expressions U_3O_7 and U_3O_8 are used to describe the tetragonal and the orthorhombic phases, while recognizing that this may not describe the exact compositions of

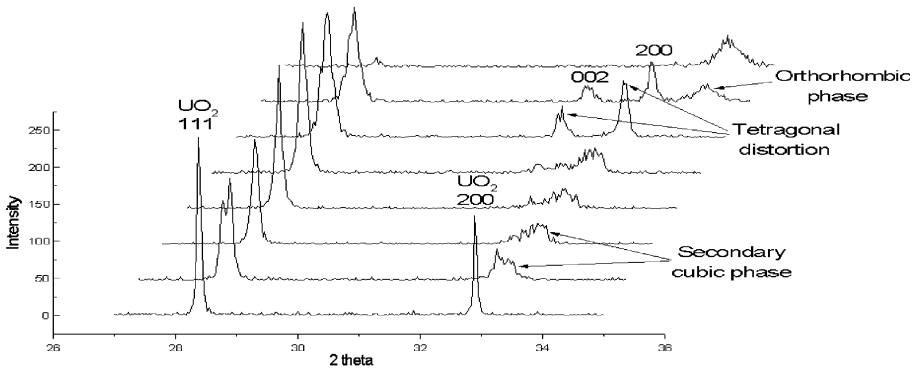

Fig. 5. Structural evolution, from ESRF experiments, during the oxidation of UO_2 into U_3O_8 at 250 °C with O_2 partial pressure equal to 0.2 atm.

these oxides. As the oxidation proceeds (Fig. 5), a splitting of the 200 peak of U_4O_{9-y} is observed, leading to a doublet (200–002); this phase is tetragonal and its cell parameters corresponds to U_3O_7. Fig. 6 shows that the amplitude of the (200–002) splitting increases.

As soon as the presence of this tetragonal phase is detected, the tetragonal cell parameters, a and c, are already well differentiated from those of UO_2 and U_4O_9. The values of $a(U_3O_7)$ and $c(U_3O_7)$ are respectively equal to 0.5426(2) nm and 0.5485(2) nm, corresponding to a c/a ratio of 1.011 when U_3O_7 appears. Then, during the oxidation, they evolve continuously to reach 0.5398(2) nm and 0.5565(2) nm respectively

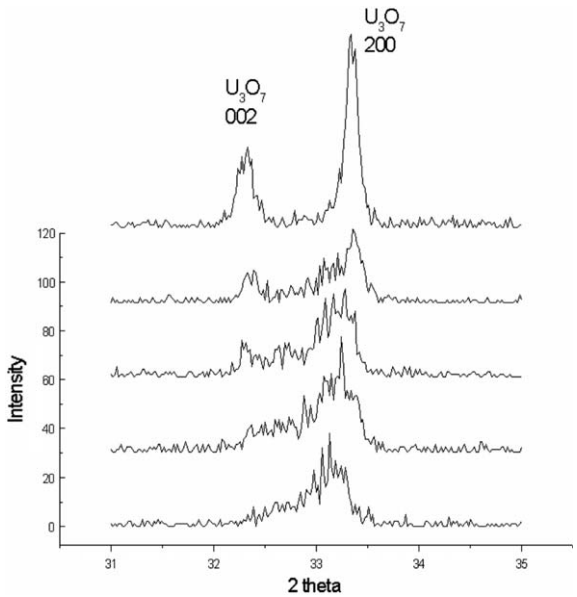

Fig. 6. Evolution of the (200–002) diffraction lines of the U_3O_7 tetragonal phase.

on the last diffraction pattern displayed in Fig. 6. These values correspond to a c/a ratio of 1.031, which equals the value for β-U_3O_7 reported by Westrum et al. [7]. Like U_4O_{9-y}, the evolution of the cell parameters during the oxidation is in good agreement with the non-stoichiometric character of U_3O_7. Like U_4O_{9-y}, the diffraction lines of U_3O_7 are also very broad, particularly in the earliest stages when the tetragonal distortion appears. However, in Fig. 6, these broad profiles of U_3O_7 tend to change continuously into sharper ones until larger amounts of β-U_3O_7 are formed. Then, the width of the diffraction lines seems to stabilise. However, in contrary to UO_2 and U_4O_9, the Rietveld analysis has not allowed us to refine the profile shapes of U_3O_7, because they present an asymmetric broadening due to the residual U_4O_{9-y} phase (Fig. 7). It is also very interesting to note that the d_{111} reticular distance is the same for U_4O_9 and U_3O_7, which shows that the crystalline structures of these two phases are still related. Like the transition from UO_2 into U_4O_9, this second step is also accompanied with a continuous decrease of the cell volume compared to UO_2 (1%).

Finally, at an O/U ratio higher than 2.33, the X-ray diffraction patterns indicate the formation of an orthorhombic U_3O_8-type phase. This evolution corresponds to the transformation from β-U_3O_7 to U_3O_8. Assuming the C2mm space group for U_3O_8, a, b and c cell parameters are found to be respectively equal to 0.6784(2) nm, 1.1890(2) nm and 0.4141(2) nm. These values are close to those already reported in the literature [30]. While the variations observed for UO_2, U_4O_9 and U_3O_7 cell parameters, are continuous, those of U_3O_8 are not. After the large discontinuity at the phase transition, the lattice parameters are almost constant

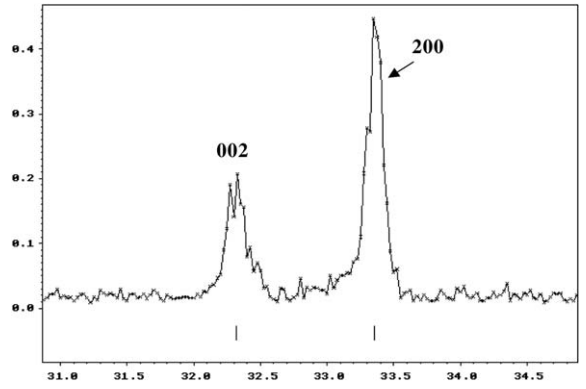

Fig. 7. Asymmetric broadening of the (200–002) diffraction lines of the U_3O_7 tetragonal phase.

until the oxidation into U_3O_8 is complete. The profile shapes of U_3O_8 are also unchanged as the oxidation of U_3O_7 proceeds. The analysis of the broadenings can be explained as plate-like diffracting domains. The measured cell volume gives a 35.6% $\Delta V/V_0$ swelling compared to UO_2, which is in good agreement with the values already reported in the literature [30]. Hence, the phase transition sequence observed in our study is as follows: UO_2 transforms into a secondary cubic phase, and then into a tetragonal phase. Finally, the U_3O_8 orthorhombic phase appears. Therefore Eq. (1) should be modified and, according to this crystalline structural study, the exact phase transition sequence is

$$UO_2 \rightarrow U_4O_{9y} \rightarrow \beta\text{-}U_3O_7 \rightarrow U_3O_8 \qquad (10)$$

The existence of the secondary cubic phase, U_4O_{9-y}, since the earliest stages of the oxidation was not mentioned in the literature, whereas an α-U_3O_7 tetragonal phase ($c/a < 1$) was reported [5,7], but definitely not observed in our study. However, the resolution of the diffraction patterns in previous experiments and the ex situ crystallographic determinations could have prevented the observation of the simultaneous splitting of all the diffraction peaks during the early stages of oxidation. This would explain the reporting of α-U_3O_7 phase in literature.

The in situ classical X-ray diffraction allowed us to determine the crystalline phases at 250 °C as a function of oxidation time domains. The first detection of U_3O_7 occurs between 1 and 2 h of oxidation whereas the characteristic diffraction peaks of U_3O_8 are detected after 6 h, as monitored by the (001) reflection at $2\theta = 21.5°$. Hence, the relationship between the time domains and the crystalline phases is illustrated in Table 2. Table 2 shows that the first

Table 2
Kinetic domains, related crystalline phases and chemical reactions

Kinetics domains	Crystalline phases
I	UO_2–U_4O_9
II	UO_2–U_4O_9–U_3O_7
III	U_3O_7–U_3O_8
IV	

kinetic domain corresponds to the reaction of UO_2 into U_4O_9, the second one is linked to the two simultaneous reactions, UO_2 into U_4O_9, and U_4O_9 into U_3O_7. Finally, the transition from U_3O_7 into U_3O_8 corresponds to the third and fourth kinetic domains.

5. Discussion

This kinetic and structural study gives a new description of the oxidation of UO_2 into U_3O_8 at 250 °C under an oxygen partial pressure of 0.2 atm. This evolution is divided in four time domains, which are discussed below.

In the first domain I, UO_2 is transformed into U_4O_9. During this reaction, the 'ΦE' test is verified. In domain I of the weight gain curve, the R_r/R_l ratio is constant and equal to 1.3 ± 0.1. This implies that a single rate-limiting step assumption is a valid modelling assumption for this transformation. This is also in good agreement with the literature, where the formation of U_4O_9 is assumed to follow a diffusion-controlled mechanism [3]. In addition, the broad profile of U_4O_9 can be interpreted as a non-stoichiometric phase resulting from the existence of an oxygen concentration gradient in the grains. This observation also agrees with the non-stoichiometric character of U_4O_9 reported in the literature [35].

For the domain II, it is necessary to consider two simultaneous reactions: UO_2, is transformed into U_4O_9, and U_4O_9 into U_3O_7. This simultaneous existence of three crystalline phases can explain why the 'ΦE' test is not experimentally verified. It also can explain the continuous evolution of the R_r/R_l ratio from 1.7 to 6.0 during the oxidation. Hence, in this domain, the approximation of a single rate-limiting step is not applicable for model developments. It seems probable that the kinetic behaviour results from a complex oxidation front. The evolution of the diffraction lines, from U_4O_9 to U_3O_7, suggests that the diffusion of oxygen inside the solid creates

continuously some defects. During the oxidation, a progressive ordering of these defects seems to appear leading finally to the formation of a well-crystallised β-U_3O_7.

The transformation of the tetragonal phase, U_3O_7 into U_3O_8, corresponds to the two last domains. For the domain III, the R_r/R_l ratio is constant and equal to 7.6 ± 0.2, which shows that the rate-limiting step is verified. However, the description of this transformation, using a nucleation and growth mechanism, does not explain why the diffracting crystallite size of U_3O_8 stays constant. It must be pointed out that the U_3O_8 crystallite sizes are the same, independently of the original grain size of the powder batch, although U_3O_8 appears for smaller O/U ratios in the smaller grains. Therefore, it seems necessary to perform additional kinetic studies to fully understand domain III.

Finally, the fourth domain remains unclear. In fact, the R_r/R_l ratio decreases from 7.1 to 5.6. This evolution shows that the rate-limiting step theory is not applicable during all the transformation of U_3O_7 into U_3O_8. However, The 'ΦE' tests may provide an explanation for the very large dispersion in the estimated values of the activation energy during U_3O_8 formation that has been reported in the literature [3].

6. Conclusion

All our experimental results at 250 °C provide strong evidence that existing models, generally adopted in the literature to describe the oxidation of UO_2 into U_3O_8, are not fully descriptive of the complex oxide phase transformations. In fact, these kinetic studies indicate four separate kinetic domains, and in only two domains a single rate-limiting step approximation was applicable for a simplified model. Moreover, the high resolution of the synchrotron diffraction provides data of four different crystalline oxide phases, and evidence of the new oxide phase transition sequence as a base for new models

$$UO_2 \rightarrow U_4O_9 \rightarrow \beta\text{-}U_3O_7 \rightarrow U_3O_8 \quad (11)$$

These results demonstrate an new and general approach for investigating rates and phases during the oxidation of uranium dioxide at temperature lower than 400 °C. In particular, the progressive transition from UO_2 into U_4O_9 and β-U_3O_7, observed in the second domain, allows a better understanding of the plateau before the formation of U_3O_8. The time duration of this plateau is an important parameter for some proposed models of uranium oxidation behaviour during long-term storage.

Acknowledgements

The authors wish to thank P. Taylor for stimulating discussions and critical review of the manuscript. They are also grateful to Electricité de France (EDF) for its financial support within the Research Program on the long-term Evolution of Spent Fuel Waste Packages of the CEA (PRECCI).

References

[1] P. Taylor, D.D. Wood, A.M. Duclos, D.G. Owen, J. Nucl. Mater. 168 (1989) 70.
[2] S. Aronson, R.B. Roof Jr., J. Belle, J. Chem. Phys. 27 (1957) 137.
[3] R.J. McEachern, P. Taylor, J. Nucl. Mater. 254 (1998) 87.
[4] P.E. Blackburn, J. Weissbart, E.A. Gulbransen, J. Phys. Chem. 62 (1958) 902.
[5] H.R. Hoekstra, A. Santoro, S. Siegel, J. Inorg. Nucl. Chem. 18 (1961) 166.
[6] L.E. Thomas, R.E. Einziger, H.C. Buchanan, J. Nucl. Mater. 201 (1993) 310.
[7] E.F. Westrum, F. Gronvold, J. Phys. Chem. Solids 23 (1962) 39.
[8] G.C. Allen, N.R. Holmes, J. Nucl. Mater. 223 (1995) 231.
[9] D.E.Y. Walker, J. Appl. Chem. 15 (1965) 128.
[10] R.J. McEachern, J.W. Choi, M. Kolar, W. Long, P. Taylor, D.D. Wood, J. Nucl. Mater. 249 (1997) 58.
[11] P. Taylor, R.J. McEachern, D.C. Doern, D.D. Wood, J. Nucl. Mater. 256 (1998) 213.
[12] J.H. Sharp et al., J. Am. Ceram. Soc. 49 (1966) 379.
[13] A.K. Galway, M.E. Brown, Thermal Decomposition of Ionic Solids, Elsevier, 1999.
[14] W. Jander, Z. Anorg. Allg. Chem. 163 (1927) 1; Angew. Chem. 41 (1928) 79.
[15] H. Schmalzried, Chemical Kinetics of Solids, VCH Publishers, 1995, p. 157.
[16] A.M. Ginstling, B.I. Brounshtein, Zh. Prikl. Khim. 23 (1950) 1327.
[17] R.E. Carter, J. Chem. Phys. 35 (1961) 1137, 2010.
[18] G. Valensi, J. Chem. Phys. 47 (1950) 489.
[19] M. Avrami, J. Chem. Phys. 7 (1939) 1103.
[20] B.V. Erofeev, C.R. Acd. Sci. URSS 52 (1946) 511.
[21] W.A. Johnson, R.F. Mehl, Trans. Am. Inst. Miner. (Metall.) Eng. 135 (1939) 416.
[22] M. Soustelle, Modélisation Macroscopique des Transformations Physico-chimiques, Masson, Paris, 1990.
[23] M. Soustelle, M. Pijolat, Solid State Ion. 95 (1997) 33.
[24] K. Surla et al., Solids State Ion. 143 (2001) 355.
[25] M. Tupin, M. Pijolat, F. Valdivieso, M. Soustelle, A. Frichet, P. Barberis, J. Nucl. Mater. 317 (2003) 130.
[26] K. Surla, F. Valdivieso, M. Pijolat, M. Soustelle, M. Prin, Ann. Chim. Sci. Mater. 25 (2000) 601.

[27] K. Nahdi, S. Perrin, M. Pijolat, F. Rouquerol, N. Ariguib, M. Ayadi, Phys. Chem. Chem. Phys. 4 (2002) 1972.
[28] B.T.M. Willis, J. Phys. 25 (1964) 431.
[29] B. Belbeoch, J.C. Boibineau, P. Perio, J. Phys. Chem. Solids 28 (1967) 1267.
[30] B.O. Loopstra, J. Appl. Cryst. 3 (1970) 94.
[31] R.A. Young, The Rietveld Method, Oxford University, 1993.
[32] V. Petricev, M. Dusek, JANA2000, Institute of Physics, Academy of Sciences of the Czech Republic, Praha, December, 2000.
[33] H.P. Klug, L.E. Alexander, X-Ray Diffraction Procedures, 2nd Ed., Wiley Interscience, 1974 (Chapter 9).
[34] I. Cohen, R.M. Berman, J. Nucl. Mater. 18 (1966) 77.
[35] D.J.M. Bevan, I.E. Grey, B.T.M. Willis, J. Solid State Chem. 61 (1986) 1.